44th AIAA Aerospace Sciences Meeting and Exhibit
9 - 12 January 2006, Reno, Nevada

AIAA 2006-697

AIAA Paper 2006-0697

Numerical Simulation of 3-D Wing Flutter with Fully Coupled Fluid-Structural Interaction

Xiangying Chen* and Ge-Cheng Zha†
Dept. of Mechanical and Aerospace Engineering
University of Miami
Coral Gables, Florida 33124

Ming-Ta Yang‡
Discipline Engineering - Structures
Pratt & Whitney
400 Main Street, M/S 163-07
East Hartford, CT 06108

Abstract

This paper describes a numerical methodology coupling Navier-Stokes equations and structural modal equations for predicating 3D transonic wing flutter. A dual-time step implicit unfactored Gauss-Seidel iteration with Roe scheme are employed for the flow solver. A modal approach is used for the structural response. The flow and structural solvers are fully coupled vis successive iterations within each physical time step. The accuracy of the modal approach structure solver is validated with finite element solver ANSYS. The results indicate that the first five modes are sufficient to accurately model the wing structure response for present study. The computed flutter boundary of AGARD wing 445.6 for free stream Mach numbers ranging from 0.499 to 1.141 agrees well with the experiment.

1 Introduction

Flutter of airplane wings or aircraft engine turbomachinery blades is a critical issue determining the reliability of the aircraft. The flutter phenomenon is the results of the fluid-structural interaction and is usually involved with complicated phenomena such as the shock wave/boundary layer interaction, flow separation, non-linear limited cycle oscillation, etc. Accurate prediction of the flutter is very challenging due to the perplexing physical phenomena and the required large amount of computation. The present study is an effort to develop the methodologies to achieve high fidelity prediction of aircraft flutter.

Among the researchers in the area of 3D aeroelastic analysis based on nonlinear flow equations in time domain, Lee-Rausch and Batina[1] used a three-factor, implicit, upwind-biased Euler/Navier-Stokes approach coupled with a modal structure solver. Morton, Melville and Gordnier et al.

* Research Associate
† Associate Professor
‡ Principal Engineer

developed an implicit fully coupled fluid-structure interaction model, which used a Beam-Warming implicit, approximate factorization scheme for the flow solver coupled with modal structural solver [2][3][4][5]. Liu et al. developed a fully coupled method using Jameson's explicit scheme with multigrid approach and a modal structural model[6]. Doi and Alonso[7] coupled an explicit Runge-Kutta multigrid flow solver with a FEM structure solver to predict the aeroelastic responses of NASA Rotor 67 blade.

Chen et al.[8, 9] have recently developed a fully coupled methodology between fluid and structure for 2-D flow-induced vibrations of rigid bodies. In their method, the Roe scheme is extended to the moving grid system. The unsteady solutions march in time by using a dual-time stepping implicit unfactored Gauss-Seidel iteration. The unsteady Navier-Stokes equations and the structural equations are fully coupled implicitly via successive iteration within each physical time step.

In present study, the method developed by Chen et al. [8, 9] is extended to 3-D flutter prediction of a transonic flexible wing. The structural response is calculated by the efficient modal approach. Comparing the different methods aforementioned for 3D aeroelastic analysis, the methodology of this paper has the the following advantages:

(1) The unfactored Gauss-Seidel iteration is unconditionally stable and allows larger pseudo or physical time steps than explicit method. It avoids the factorization error introduced by those implicit factorized methods, such as the methods used in [1][2][3][4][5]. Even though the factorization error is diminished within each physical time step, the factorization error can limit the numerical stability.

(2) Unlike the central differencing schemes used in [2] [2][3][4][5][6], the Roe scheme has its inherent dissipation, and does not need additional artificial dissipation, which may need to be calibrated case by case. The adjusted numerical dissipation may significantly affect the flow damping to the structural response.

The objective of this paper is to apply the developed methodology to 3D transonic wing flutter prediction. The results indicate that the present methodology predicts the flutter boundary in good agreement with the experiment.

2 CFD Aerodynamic Model

2.1 Flow Governing Equations

The governing equations for the flow field computation are the Reynolds-Averaged Navier-Stokes equations (RANS) with Favre mass average which can be transformed to the generalized coordinates and expressed as:

$$\frac{\partial \mathbf{Q}'}{\partial t} + \frac{\partial \mathbf{E}'}{\partial \xi} + \frac{\partial \mathbf{F}'}{\partial \eta} + \frac{\partial \mathbf{G}'}{\partial \zeta} = \frac{1}{Re}\left(\frac{\partial \mathbf{E}'_{\mathbf{v}}}{\partial \xi} + \frac{\partial \mathbf{F}'_{\mathbf{v}}}{\partial \eta} + \frac{\partial \mathbf{G}'_{\mathbf{v}}}{\partial \zeta}\right) \tag{1}$$

where Re is the Reynolds number and

$$\mathbf{Q}' = \frac{\mathbf{Q}}{J} \tag{2}$$

$$\mathbf{E}' = \frac{1}{J}(\xi_t \mathbf{Q} + \xi_x \mathbf{E} + \xi_y \mathbf{F} + \xi_z \mathbf{G}) = \frac{1}{J}(\xi_t \mathbf{Q} + \mathbf{E}'') \tag{3}$$

$$\mathbf{F}' = \frac{1}{J}(\eta_t \mathbf{Q} + \eta_x \mathbf{E} + \eta_y \mathbf{F} + \eta_z \mathbf{G}) = \frac{1}{J}(\eta_t \mathbf{Q} + \mathbf{F}'') \tag{4}$$

$$\mathbf{G}' = \frac{1}{J}(\zeta_t \mathbf{Q} + \zeta_x \mathbf{E} + \zeta_y \mathbf{F} + \zeta_z \mathbf{G}) = \frac{1}{J}(\zeta_t \mathbf{Q} + \mathbf{G}'') \tag{5}$$

$$\mathbf{E}'_{\mathbf{v}} = \frac{1}{J}(\xi_x \mathbf{E}_{\mathbf{v}} + \xi_y \mathbf{F}_{\mathbf{v}} + \xi_z \mathbf{G}_{\mathbf{v}}) \tag{6}$$

$$\mathbf{F}'_{\mathbf{v}} = \frac{1}{J}(\eta_x \mathbf{E}_{\mathbf{v}} + \eta_y \mathbf{F}_{\mathbf{v}} + \eta_z \mathbf{G}_{\mathbf{v}}) \tag{7}$$

$$\mathbf{G}'_{\mathbf{v}} = \frac{1}{J}(\zeta_x \mathbf{E}_{\mathbf{v}} + \zeta_y \mathbf{F}_{\mathbf{v}} + \zeta_z \mathbf{G}_{\mathbf{v}}) \tag{8}$$

where the variable vector $\mathbf{Q}$, and inviscid flux vectors $\mathbf{E}$, $\mathbf{F}$, and $\mathbf{G}$ are

$$\mathbf{Q} = \begin{pmatrix} \bar{\rho} \\ \bar{\rho}\tilde{u} \\ \bar{\rho}\tilde{v} \\ \bar{\rho}\tilde{w} \\ \bar{\rho}\tilde{e} \end{pmatrix}, \mathbf{E} = \begin{pmatrix} \bar{\rho}\tilde{u} \\ \bar{\rho}\tilde{u}\tilde{u} + \tilde{p} \\ \bar{\rho}\tilde{u}\tilde{v} \\ \bar{\rho}\tilde{u}\tilde{w} \\ (\bar{\rho}\tilde{e} + \tilde{p})\tilde{u} \end{pmatrix}, \mathbf{F} = \begin{pmatrix} \bar{\rho}\tilde{v} \\ \bar{\rho}\tilde{u}\tilde{v} \\ \bar{\rho}\tilde{v}\tilde{v} + \tilde{p} \\ \bar{\rho}\tilde{w}\tilde{v} \\ (\bar{\rho}\tilde{e} + \tilde{p})\tilde{v} \end{pmatrix}, \mathbf{G} = \begin{pmatrix} \bar{\rho}w \\ \bar{\rho}\tilde{u}\tilde{w} \\ \bar{\rho}\tilde{v}\tilde{w} \\ \bar{\rho}\tilde{w}\tilde{w} + \tilde{p} \\ (\bar{\rho}\tilde{e} + \tilde{p})\tilde{w} \end{pmatrix},$$

The $\mathbf{E}''$, $\mathbf{F}''$, and $\mathbf{G}''$ are the inviscid fluxes at the stationary grid system and can be expressed as

$$\mathbf{E}'' = \xi_x \mathbf{E} + \xi_y \mathbf{F} + \xi_z \mathbf{G},$$

$$\mathbf{F}'' = \eta_x \mathbf{E} + \eta_y \mathbf{F} + \eta_z \mathbf{G},$$

$$\mathbf{G}'' = \zeta_x \mathbf{E} + \zeta_y \mathbf{F} + \zeta_z \mathbf{G},$$

and the viscous flux vectors are given by

$$\mathbf{E}_{\mathbf{v}} = \begin{pmatrix} 0 \\ \bar{\tau}_{xx} - \overline{\rho u'' u''} \\ \bar{\tau}_{xy} - \overline{\rho u'' v''} \\ \bar{\tau}_{xz} - \overline{\rho u'' w''} \\ Q_x \end{pmatrix}, \mathbf{F}_{\mathbf{v}} = \begin{pmatrix} 0 \\ \bar{\tau}_{yx} - \overline{\rho v'' u''} \\ \bar{\tau}_{yy} - \overline{\rho v'' v''} \\ \bar{\tau}_{yz} - \overline{\rho v'' w''} \\ Q_y \end{pmatrix}, \mathbf{G}_{\mathbf{v}} = \begin{pmatrix} 0 \\ \bar{\tau}_{zx} - \overline{\rho w'' u''} \\ \bar{\tau}_{zy} - \overline{\rho w'' v''} \\ \bar{\tau}_{zz} - \overline{\rho w'' w''} \\ Q_z \end{pmatrix}$$

In above equations, ρ is the density, u, v, and w are the Cartesian velocity components in x, y and z directions, p is the static pressure, and e is the total energy per unit mass. The overbar denotes the Reynolds-averaged quantity, tilde and double-prime denote the Favre mean and Favre

fluctuating part of the turbulent motion respectively. All the flow variable in above equations are non-dimensionlized by using the freestream quantities and a reference length L.

Let subscript 1, 2 and 3 represent the coordinates, x, y, and z, and use Einstein summation convention, the shear-stress and Q_x, Q_y, Q_z terms in non-dimensional forms can be expressed in tensor form as

$$\bar{\tau}_{ij} = -\frac{2}{3}\tilde{\mu}\frac{\partial \tilde{u}_k}{\partial x_k}\delta_{ij} + \tilde{\mu}(\frac{\partial \tilde{u}_i}{\partial x_j} + \frac{\partial \tilde{u}_j}{\partial x_i}) \tag{9}$$

$$Q_i = \tilde{u}_j(\bar{\tau}_{ij} - \overline{\rho u'' u''}) - (\bar{q}_i + C_p\overline{\rho T'' u_i''}) \tag{10}$$

where the mean molecular heat flux is

$$\bar{q}_i = -\frac{\tilde{\mu}}{(\gamma-1)Pr}\frac{\partial a^2}{\partial x_i} \tag{11}$$

The molecular viscosity $\tilde{\mu} = \tilde{\mu}(\tilde{T})$ is determined by Sutherland law, and $a = \sqrt{\gamma R T_\infty}$ is the speed of sound. The equation of state closes the system,

$$\bar{\rho}\tilde{e} = \frac{\tilde{p}}{(\gamma-1)} + \frac{1}{2}\bar{\rho}(\tilde{u}^2 + \tilde{v}^2 + \tilde{w}^2) + k \tag{12}$$

where γ is the ratio of specific heats, k is the Favre mass-averaged turbulence kinetic energy. The turbulent shear stresses and heat flux appeared in above equations are calculated by Baldwin-Lomax model[10]. The viscosity is composed of $\mu + \mu_t$, where μ is the molecular viscosity and μ_t is the turbulent viscosity determined by Baldwin Lomax model. For a laminar flow, the μ_t is set to be zero.

2.2 Time Marching Scheme

The time dependent governing equation (1) is solved using the control volume method with the concept of dual time stepping suggested by Jameson[11]. A pseudo temporal term $\frac{\partial \mathbf{Q}}{\partial \tau}$ is added to the governing equation (1). This term vanishes at the end of each physical time step, and has no influence on the accuracy of the solution. However, instead of using the explicit scheme as in [11], an implicit pseudo time marching scheme using line Gauss-Seidel iteration is employed to achieve high CPU efficiency. For unsteady time accurate computations, the temporal term is discretized implicitly using a three point, backward differencing as the following

$$\frac{\partial \mathbf{Q}}{\partial t} = \frac{3Q^{n+1} - 4Q^n + Q^{n-1}}{2\Delta t} \tag{13}$$

Where n is the time level index. The pseudo temporal term is discretized with first order Euler scheme. Let m stand for the iteration index within a physical time step, the semi-discretized governing equation (1) can be expressed as

$$[(\frac{1}{\Delta\tau} + \frac{1.5}{\Delta t})I - (\frac{\partial R}{\partial Q})^{n+1,m}]\delta Q^{n+1,m+1} = R^{n+1,m} - \frac{3Q^{n+1,m} - 4Q^n + Q^{n-1}}{2\Delta t} \tag{14}$$

where the $\Delta\tau$ is the pseudo time step, R is the net flux going through the control volume,

$$R = -\frac{1}{V}\int_s [(F - F_v)\mathbf{i} + (G - G_v)\mathbf{j} + (H - H_v)\mathbf{k}]\cdot d\mathbf{s} \tag{15}$$

where V is the volume of the control volume, $\mathbf{s}$ is the control volume surface area vector. Equation (14) is solved using the unfactored line Gauss-Seidel iteration. The method is unconditionally stable and can reach very large pseudo time step since no factorization error is introduced.

2.3 Roe's Riemann Solver on Moving Grid System

An accurate Riemann solver is necessary to resolve the shock wave and wall boundary layer in the flow field. The Roe scheme[12] is selected and implemented in the code to evaluate the inviscid fluxes with the 3rd order MUSCL type differencing[13]. In present study, the original Roe scheme is extended to moving grid system as the following, for example, in ξ direction:

$$\mathbf{E}'_{i+\frac{1}{2}} = \frac{1}{2}[\mathbf{E}''(\mathbf{Q_L}) + \mathbf{E}''(\mathbf{Q_R}) + \mathbf{Q_L}\xi_{tL} + \mathbf{Q_R}\xi_{tR} - |\tilde{\mathbf{A}}|(\mathbf{Q_R} - \mathbf{Q_L})]_{i+\frac{1}{2}} \tag{16}$$

where $\mathbf{Q_L}$ and $\mathbf{Q_R}$ are the reconstructed variables to the left and right sides of the cell face, ξ_{tL} and ξ_{tR} are the reconstructed grid velocity component in ξ direction to the left and right sides of the cell interface $i + \frac{1}{2}$, $\mathbf{A}$ is the Jacobian matrix, $\mathbf{A} = \frac{\partial \mathbf{E}'}{\partial \mathbf{Q}}$ and it takes the form as $\mathbf{A} = \mathbf{T}\mathbf{\Lambda}\mathbf{T}^{-1}$, $\mathbf{T}$ is the right eigenvector matrix of $\mathbf{A}$, $\mathbf{\Lambda}$ is the eigenvalue matrix of $\mathbf{A}$, and

$$\tilde{\mathbf{A}} = \tilde{\mathbf{T}}\tilde{\mathbf{\Lambda}}\tilde{\mathbf{T}}^{-1} \tag{17}$$

where $\tilde{\mathbf{\Lambda}}$ is the eigenvalue matrix on moving grid system with the eigenvalues of

$$(\tilde{U} + \tilde{C}, \tilde{U} - \tilde{C}, \tilde{U}, \tilde{U}, \tilde{U}) \tag{18}$$

where $\tilde{U}$ is the contravariant velocity in ξ direction on moving grid,

$$\tilde{U} = \tilde{\xi}_t + \xi_x\tilde{u} + \xi_y\tilde{v} + \xi_z\tilde{w} \tag{19}$$

$\tilde{C}$ is the speed of sound corresponding to the contravariant velocity:

$$\tilde{C} = \tilde{c}\sqrt{\xi_x^2 + \xi_y^2 + \xi_z^2} \tag{20}$$

where $c = \sqrt{\gamma RT}$ is the physical speed of sound. The $\sim$ stands for the Roe-averaged quantities. For example,

$$\tilde{\xi}_t = (\xi_{tL} + \xi_{tR}\sqrt{\rho_R/\rho_L})/(1 + \sqrt{\rho_R/\rho_L}) \tag{21}$$

It can be proved that the eigenvector matrix $\mathbf{T}$ is exactly the same as the one without moving grid. The only difference between the moving grid and the stationary grid system is that, for the moving grid system, the contravariant velocity in the eigenvalues contains the grid velocity as given

in Equation (19). It is hence straightforward to extend the code from a stationary grid system to the moving grid system using Roe scheme without major change.

The grid velocity is evaluated at the center of each cell and is determined by the averaged value that counts all the movement at eight vertexes if hexahedral control volumes are used. The grid velocity is reconstructed with 3rd MUSCL differencing.

2.4 Boundary Conditions

The boundary conditions for the computation of wing flutter are as follows:

(1) Upstream boundary conditions: The outer boundary is divided into upstream and downstream boundaries according to whether the direction of its segment is toward or backward to the incoming flow direction. On upstream boundary, it is assumed that the streamwise velocity u is uniform, transverse velocity $v = 0$, and spanwise velocity $w = 0$. Other primitive variables are specified according to the freestream condition except the pressure which is extrapolated from interior.

(2) Downstream boundary conditions: All the flow quantities are extrapolated from interior except the pressure which is set to be its freestream value.

(3) Solid wall boundary conditions: At moving boundary surface, the no-slip condition is enforced by extrapolating the velocity between the phantom and interior cells,

$$u_0 = 2\dot{x}_b - u_1, \qquad v_0 = 2\dot{y}_b - v_1, \qquad w_0 = 2\dot{z}_b - w_1 \tag{22}$$

where u_0, v_0 and w_0 denote the velocity at phantom cell, u_1, v_1 and w_1 denote the velocity at the $1st$ interior cell close to the boundary, and u_b, v_b and w_b are the velocity on the moving boundary.

If the wall surface is in η direction, the other two conditions to be imposed on the solid wall are the adiabatic wall condition and the inviscid normal momentum equation[2] as follows,

$$\frac{\partial T}{\partial \eta} = 0, \qquad \frac{\partial p}{\partial \eta} = -\left(\frac{\rho}{\eta_x^2 + \eta_y^2 + \eta_z^2}\right)(\eta_x \ddot{x}_b + \eta_y \ddot{y}_b + \eta_z \ddot{z}_b) \tag{23}$$

2.5 Moving/Deforming Grid Systems

In the fully-coupled computation, the remeshing procedure is performed in each iteration. Therefore, a CPU time efficient algebraic grid deformation method is employed in the computation instead of the commonly-used grid generation method in which the Poisson equation is solved for grid points. This grid deformation procedure is designed in such a way that the far-field boundary is held fixed, and the grids on the wing surface are moving and deforming in accordance with the instantaneous motion of the wing structure. Then the grids between the wing surface and the far-field boundary can be obtained by using a non-linear interpolation. This simple remeshing strategy is proved to be robust for all the cases investigated in present study. By monitoring the accuracy criterion y^+, it is shown that the method can maintain the initial grid quality and keep almost same mesh refinement around the wing surface.

2.6 Geometric Conservation Law

It was pointed out by Thomas et al.[14] that due to the mixed temporal and spatial derivatives after discretization, an additional term appears, which theoretically equals to zero but numerically still remains. Consequently numerical error could be introduced in the discretized form of the equations of the flow motion if this term is neglected. In order to reduce or avoid this error, the geometric conservation law needs to be enforced. In other words, the following additional term should be added to the right-hand side of the equations as a source term:

$$\mathbf{S} = \mathbf{Q}\left[\frac{\partial J^{-1}}{\partial t} + \left(\frac{\xi_t}{J}\right)_\xi + \left(\frac{\eta_t}{J}\right)_\eta + \left(\frac{\zeta_t}{J}\right)_\zeta\right] \tag{24}$$

To implement this option in the flow solver, the source term is then linearized such that

$$\mathbf{S}^{n+1} = \mathbf{S}^n + \frac{\partial \mathbf{S}}{\partial \mathbf{Q}}\Delta\mathbf{Q}^{n+1} \tag{25}$$

As has been observed, the overall performance of this numerical supplement is beneficial with very little CPU time cost.

3 Structural Model of Three Dimensional Wing

3.1 Modal Approach

The governing equation of motion of the solid structure can be written as,

$$\mathbf{M}\frac{d^2\mathbf{u}}{dt^2} + \mathbf{C}\frac{d\mathbf{u}}{dt} + \mathbf{K}\mathbf{u} = \mathbf{f} \tag{26}$$

where $\mathbf{M}$, $\mathbf{C}$ and $\mathbf{K}$ are the mass, damping, and stiffness matrices of the solid respectively, $\mathbf{u}$ is the displacement vector and $\mathbf{f}$ is the force exerted on the surface node points of the solid, both can be expressed as:

$$\mathbf{u} = \begin{pmatrix} \mathbf{u}_1 \\ \vdots \\ \mathbf{u}_i \\ \vdots \\ \mathbf{u}_N \end{pmatrix}, \mathbf{f} = \begin{pmatrix} \mathbf{f}_1 \\ \vdots \\ \mathbf{f}_i \\ \vdots \\ \mathbf{f}_N \end{pmatrix},$$

where N is the total number of node points of the structural model, $\mathbf{u}_i$ and $\mathbf{f}_i$ are

$$\mathbf{u}_i = \begin{pmatrix} \mathbf{u}_{ix} \\ \mathbf{u}_{iy} \\ \mathbf{u}_{iz} \end{pmatrix}, \mathbf{f}_i = \begin{pmatrix} \mathbf{f}_{ix} \\ \mathbf{f}_{iy} \\ \mathbf{f}_{iz} \end{pmatrix}.$$

The displacement and force vectors at node point i, $\mathbf{u}_i$, $\mathbf{f}_i$, have three components in three dimensional space. $\mathbf{f}_i$ is dynamic force exerted on the surface of the solid body. In a modal approach, the modal decomposition of the structure motion can be expressed as follows:

$$\mathbf{K\Phi} = \mathbf{M\Phi\Lambda} \tag{27}$$

or

$$\mathbf{K}\phi_j = \lambda_j \mathbf{M}\phi_j \tag{28}$$

where $\mathbf{\Lambda}$ is eigenvalue matrix, $\mathbf{\Lambda} = diag[\lambda_1, \cdots, \lambda_j, \cdots, \lambda_{3N}]$, and jth eigenvalue $\lambda_j = {\omega_j}^2$, ω_j is natural frequency of jth mode, and the mode shape matrix $\mathbf{\Phi} = [\phi_1, \cdots, \phi_j, \cdots, \phi_{3N}]$.

Equation (28) can be solved by using finite element solver (e.g. ANSYS) to obtain its finite number of mode shapes ϕ_j. The first five mode shapes will be used in this paper to calculate the displacement of the structure such that,

$$\mathbf{u}(t) = \sum_j a_j(t)\phi_j = \mathbf{\Phi a} \tag{29}$$

where $\mathbf{a} = [a_1, a_2, a_3, \cdots]^T$. Substitute Equation (29) to Equation (26) and yield

$$\mathbf{M\Phi}\frac{d^2\mathbf{a}}{dt^2} + \mathbf{C\Phi}\frac{d\mathbf{a}}{dt} + \mathbf{K\Phi a} = \mathbf{f} \tag{30}$$

Multiply Equation (30) by $\mathbf{\Phi}^T$ and re-write it as

$$\hat{\mathbf{M}}\frac{d^2\mathbf{a}}{dt^2} + \hat{\mathbf{C}}\frac{d\mathbf{a}}{dt} + \hat{\mathbf{K}}\mathbf{a} = \mathbf{P} \tag{31}$$

where $\mathbf{P} = [P_1, P_2, \cdots, P_j, \cdots]^T$, the modal force of jth mode, $P_j = \phi_j^T \mathbf{f}$, the modal mass matrix is defined as

$$\hat{\mathbf{M}} = \mathbf{\Phi}^T\mathbf{M\Phi} = diag(m_1, \cdots, m_j, \cdots, m_{3N}) \tag{32}$$

where m_j is the modal mass of jth mode, and the modal damping matrix is defined as

$$\hat{\mathbf{C}} = \mathbf{\Phi}^T\mathbf{C\Phi} = diag(c_1, \cdots, c_j, \cdots, c_{3N}) \tag{33}$$

where c_j is the modal damping of jth mode, and the modal stiffness matrix is defined as

$$\hat{\mathbf{K}} = \mathbf{\Phi}^T\mathbf{K\Phi} = diag(k_1, \cdots, k_j, \cdots, k_{3N}) \tag{34}$$

where k_j is the modal stiffness of jth mode. Equation (31) implies

$$\frac{d^2a_j}{dt^2} + 2\zeta_j\omega_j\frac{da_j}{dt} + \omega_j^2 a_j = \frac{\phi_j^T\mathbf{f}}{m_j} \tag{35}$$

where ζ_j is modal damping ratio. Equation (35) is the modal equation of structure motion, and is solved numerically within each iteration. By carefully choosing reference quantities, the normalized equation may be expressed as

$$\frac{d^2 a_j}{dt^{*2}} + 2\zeta_j \left(\frac{\omega_j}{\omega_\alpha}\right) \frac{da_j}{dt^*} + \left(\frac{\omega_j}{\omega_\alpha}\right)^2 a_j = \phi_j^{*T} \mathbf{f}^* V^* \left(\frac{b_s}{L}\right)^2 \frac{\bar{m}}{v^*} \tag{36}$$

where the dimensionless quantities are denoted by an asterisk, ω_α is the natural frequency in pitch, b_s is the streamwise semichord measured at wing root, L is the reference length, $\bar{m}$ is the measured wing panel mass, v^* is the volume of a conical frustum having streamwise root chord as lower base diameter, streamwise tip chord as upper base diameter, and panel span as height, $V^* = \frac{U_\infty}{b_s \omega_\alpha \sqrt{\bar{\mu}}}$, and U_∞ is the freestream velocity.

Then the equations are transformed to a state form and expressed as:

$$[\mathbf{M}] \frac{\partial \{\mathbf{S}\}}{\partial t} + [\mathbf{K}]\{\mathbf{S}\} = \mathbf{q} \tag{37}$$

where

$$\mathbf{S} = \begin{pmatrix} a_j \\ \dot{a}_j \end{pmatrix}, \mathbf{M} = [I], \mathbf{K} = \begin{pmatrix} 0 & -1 \\ \left(\frac{\omega_j}{\omega_\alpha}\right)^2 & 2\zeta \left(\frac{\omega_j}{\omega_\alpha}\right) \end{pmatrix}, \mathbf{q} = \begin{pmatrix} 0 \\ \phi_j^{*T} \mathbf{f}^* V^* \left(\frac{b_s}{L}\right)^2 \frac{\bar{m}}{v^*} \end{pmatrix}.$$

To couple the structural equations with the equations of flow motion and solve them implicitly in each physical time step, above equations are discretized and integrated in a manner consistent with Equation (14) to yield

$$\left(\frac{1}{\Delta\tau}\mathbf{I} + \frac{1.5}{\Delta t}\mathbf{M} + \mathbf{K}\right) \delta S^{n+1,m+1} = -\mathbf{M} \frac{3\mathbf{S}^{n+1,m} - 4\mathbf{S}^n + \mathbf{S}^{n-1}}{2\Delta t} - \mathbf{K}\mathbf{S}^{n+1,m} + \mathbf{q}^{n+1,m+1} \tag{38}$$

where n is the physical time level index while m stands for the pseudo time index. The detailed coupling procedure between the fluid and structural systems is given in the following.

4 Fully Coupled Fluid-Structural Interaction Procedure

To rigorously simulate fluid-structural interactions, the equations of flow motion and structural response need to be solved simultaneously within each iteration in a fully coupled numerical model. The calculation based on fully coupled iteration is CPU expensive, especially for three dimensional applications. The modal approach can save CPU time significantly by solving modal displacement equations, Equation (35), instead of the original structural equations, Equation (28), which is usually solved by using finite element method. In the modal approach, the structural mode shapes can be pre-determined by using a separate finite element structural solver. Once the several mode shapes of interest are obtained, the physical displacements can be calculated just by solving those simplified linear equations, Equation (35) and Equation (29). In present study, the first five mode shapes provided in Ref.[15] are used to model the wing structure. these pre-calculated mode shapes are obtained on a fixed structural grid system, and transformed to the CFD grid system by using a 3rd order polynomial fitting procedure. The procedure is only performed once and then the mode shapes for CFD grid system are stored in the code throughout the simulation.

The procedure of fluid-structure interaction by modal approach is described as follows:

(1) The flow solver provides dynamic forces on solid surfaces.

(2) Integrate fluid forces at each surface element to derive forcing vector $\mathbf{f}$.

(3) Use Equation (35) to calculate modal displacements $a_j (j = 1, 2, 3, \cdots)$ of the next pseudo time step.

(4) Use Equation (29) to calculate physical displacement $\mathbf{u}$ of the next pseudo time step.

(5) Check the maximum residuals for both solutions of the flow and the structural equations. If the maximum residuals are greater than the prescribed convergence criteria, go back to step (1) and proceed to the next pseudo time. Otherwise the flow field and the movement of the moving object are calculated and the next new physical time step starts. The procedure can be also seen in the flow chart given in Figure 1.

5 Results and Discussion

The result of steady state transonic ONERA M6 wing is calculated first in order to validate the 3-D CFD solver. Then a plate wing is calculated numerically to validate the structural solver with the modal approach. Finally, the flutter boundary of an AGARD wing 445.6 is calculated.

5.1 Steady State Transonic ONERA M6 wing

As a validation of the three dimensional solver for a transonic wing, the steady state solution of the transonic ONERA M6 wing is calculated first since the experimental data is available for comparison. The freestream conditions for this study are listed in Table 1 below.

Table 1: Free-stream condition for ONERA M6 wing

Mach number	Static Pressure (psia)	Temperature (R)	Angle-of-Attack (deg)	Reynolds Number
0.8395	12.2913	447.0	0.0	19.7×10^6

The Roe scheme [12] is used to evaluate the inviscid fluxes with the 3rd order MUSCL type differencing [13]. The turbulent Reynolds stress and heat flux are calculated by the Baldwin-Lomax algebraic model[10]. This case is run using an O-type grid with the dimension of 144 (around wing) $\times$60 (normal to the wing) $\times$40 (spanwise). The far field boundary is located 15 chords away from the chord center of the wing. The surface mesh of the wing is depicted in Figure (2).

The computed surface pressure distributions at various cross sections are shown in Figure (3), together with the experimental data by Schmitt et al. [16]. Overall, very good agreement is obtained between the computation and experiment for each cross-section.

5.2 Validation of Structural Solver

To validate the structural model used in the present study, the dynamic responses of a flexible plate wing shown in Figure (4) is calculated and compared with the results by using finite element solver ANSYS. The plate wing has the same outline as the AGARD wing 445.6, and its first mode natural vibration frequency is nearly the same as the corresponding one of the AGARD wing 445.6. The plate wing consists of 80 elements and 861 node points on each side of the wing. The plate wing is held fixed on the root. A time- dependent force is exerted at node point 510 which is located at the mid-point of the wing tip. The three components of the force are:

$$f_x = 0.5sin(2\pi f_e t), \qquad f_y = 0.3sin(2\pi f_e t), \qquad f_z = 0.8sin(2\pi f_e t) \tag{39}$$

where the exciting frequency f_e is equal to 10 Hz. The modal damping ratio $\zeta_j = 0.01$, the time step used is 0.0005 *second*. The dynamic responses at several locations are recorded. Figure (5) presents the time histories of the responses at the node point 491 which is located almost at the center of the plate wing. The numerical predictions by present structural solver with first five mode shapes agree excellently with the results using ANSYS with first five mode shapes as well as full model. The two results are virtually duplicated to each other.

5.3 AGARD Wing 445.6 Flutter

The AGARD 445.6 wing is selected to demonstrate the capability of the present solver for predicting the flutter boundary. This wing has a quarter-chord sweep angle of 45 degree, an aspect ratio of 1.65, a taper ratio of 0.6576, and a NACA65A004 airfoil section in the streamwise direction. The weakened wing model (Model 3) listed in [15] is chosen for this study. The geometry of the wing and its first six mode shapes as well as the experimental flutter results are also provided in the same report [15]. The wing structure is modeled by its first five natural vibration modes in the present computation.

The simulations start with the stationary rigid body wing model. After the steady state flow field around the wing is fully developed, the rigid body wing is switched to the flexible wing model. As a small imposed perturbation, the first mode displacement of the structural motion is set into sinusoidal motion for one cycle with the maximum amplitude of 0.0005 - 0.001 and the first mode frequency of the wing. Then the wing is allowed to deflect in response to the dynamic force load.

In Figures (6) through (8) the time histories of generalized displacements of the AGARD wing 445.6 at $M_\infty = 0.96$ are plotted for three different V^*. In these figures, from $V^* = 0.28$ to $V^* = 0.315$, the plots correspond to the damped, neutral, and diverging responses, respectively. When the value of V^* is smaller than the critical value on the flutter boundary, the amplitudes of all modes decrease in time corresponding to the damped response as shown in Figure (6). Once the value of V^* coincides with or closes to the critical value, the neutral response appears as shown in Fig. (7). When the value of V^* is beyond the neutral stability point, the amplitudes of first five modes grow very fast, a diverging response is expected as shown in Fig. (8). At $M_\infty = 0.96$, the location of the predicated flutter boundary is about 0.29 which is consistent with the experimental value of 0.3076 provided by Ref.[15].

For a given Mach number, several runs with different V^* are needed to determine the location of the flutter boundary using bisection method. When V^* is varied, the free-stream Reynolds number is changed accordingly. Strictly, the free-stream Reynolds number needs to be updated and the

initial steady-state flow field with actual Reynolds number should be re-generated for each run. In present simulation, the Reynolds number and initial flow field remain unchanged when V^* is varied since the effect on final solution due to small variation in the free-stream Reynolds number is negligible when a turbulence model is used.

Figure (9) through (11) show the pressure distributions on the wing surface at three different moments when the wing tip is located at uppermost, neutral and lowermost positions respectively, when $M_\infty = 0.96$ and $V^* = 0.29$.

The comparison of computed flutter boundary and experimental data for AGARD Wing 445.6 is depicted in Figure (12). Overall, the computed results are in good agreement with the experimental data, especially for free-stream Mach number below 1.072. The "sonic dip" measured in the experiment is very well captured by the computation. The largest discrepancy between computed results and experimental data can be seen at $M_\infty = 1.171$, which is previously noted by other researchers[1][17]. It may be due to the inadequency of the turbulent modeling to capture the shock/wave boundary layer interaction at high Mach number with stronger shock waves.

6 Conclusion

A numerical methodology with fully coupled fluid-structural interaction for predicating 3-D transonic wing flutter has been developed. A dual-time step implicit unfactored Gauss-Seidel iteration with Roe scheme are employed for the flow solver. A modal approach is used for the structural response. The flow and structural solver are fully coupled vis successive iterations within each physical time step.

The accuracy of the modal approach structure solver has been verified with finite element solver ANSYS. The results indicate that the first five modes are sufficient to accurately model the wing structure for the present study.

The computed flutter boundary of AGARD wing 445.6 for free stream Mach numbers ranging from 0.499 to 1.141 is presented and compared well with the experimental data. The sonic dip is very well captured.

7 Acknowledgment

This work is supported by AFOSR Grant F49620-03-1-0253 monitored by Dr. Fariba Fahroo.

References

[1] E. Lee-Rausch and J. Batina, "Calculation of AGARD Wing 445.6 Flutter Using Navier-Stokes Aerodynamics." AIAA Paper 93-3476, 1993.

[2] S. A. Morton, R. B. Melville, and M. R. Visbal, "Accuracy and Coupling Issues of Aeroelastic Navier-Stokes Solutions on Deforming Meshes." AIAA Paper-97-1085, 1997.

[3] R. B. Melville, S. A. Morton, and D. P. Rizzetta, "Implementation of a Fully-Implicit, Aeroelastic Navier-Stokes Solver." AIAA Paper-97-2039, 1997.

[4] R. B. Melville and S. A. Morton, "Fully Implicit Aeroelasticity on Oveerset Grid Systems ." AIAA Paper-98-0521, 1998.

[5] R. Gordnier and M. R.B., "Transonic Flutter Simulations Using an Implicit Aeroelastic Solver," *Journal of Aircraft*, vol. 37, pp. 872–879, September-October 2000.

[6] F. Liu, J. Cai, Y. Zhu, A. Wong, and H. Tsai, "Calculation of Wing Flutter by a Coupled CFD-CSD Method." AIAA-2000-0907, 2000.

[7] H. Doi and J. Alonso, "Fluid/Structure Coupled Aeroelastic Computations for Transonic Flows in Turbomachinery." ASME Turbo Expo 2002, GT-2002-30313, 2002.

[8] X.-Y. Chen, G.-C. Zha, and Z.-J. Hu, "Numerical Simulation of Flow Induced Vibration Based on Fully Coupled-Structural Interactions." AIAA Paper 2004-2240, Juun 28 - July 1, 2004.

[9] X. Chen and G.-C. Zha, "Fully Coupled Fluid-Structural Interactions Using an Efficient High Solution Upwind Scheme," *Journal of Fluid and Structure*, vol. 20, pp. 1105–1125, 2005.

[10] B. Baldwin and H. Lomax, "Thin-Layer Approximation and Algebraic Model for Separated Turbulent flows." AIAA Paper 78-257, 1978.

[11] A. Jameson, "Time Dependent Calculations Using Multigrid with Application to Unsteady Flows past Airfoils and Wings." AIAA Paper 91-1596, 1991.

[12] P. Roe, "Approximate Riemann Solvers, Parameter Vectors, and Difference Schemes," *Journal of Computational Physics*, vol. 43, pp. 357–372, 1981.

[13] B. Van Leer, "Towards the Ultimate Conservative Difference Scheme, III," *Journal of Computational Physics*, vol. 23, pp. 263–75, 1977.

[14] P. Thomas and C. Lombard, "Geometric Conservation Law and Its Application to Flow Computations on Moving Grids," *AIAA Journal*, vol. 17, pp. 1030–1037, 1979.

[15] E. Yates Jr., "Agard standard aeroelastic configurations for dynamic response i.-wing 445.6," Tech. Rep. AGARD Report No.765, AGARD, September 1985.

[16] V. Schmitt and F. Charpin, "Pressure Distributions on the onera-m6-wing at Transonic Mach Numbers," Tech. Rep. AGARD AR 138, AGARD, May 1979.

[17] F. Liu, Y. Zhu, H. Tsai, and A. Wong, "Calculation of Wing Flutter by a Coupled Fluid-Structure Method," *Journal of Aircraft*, vol. 38, pp. 334–342, 2001.

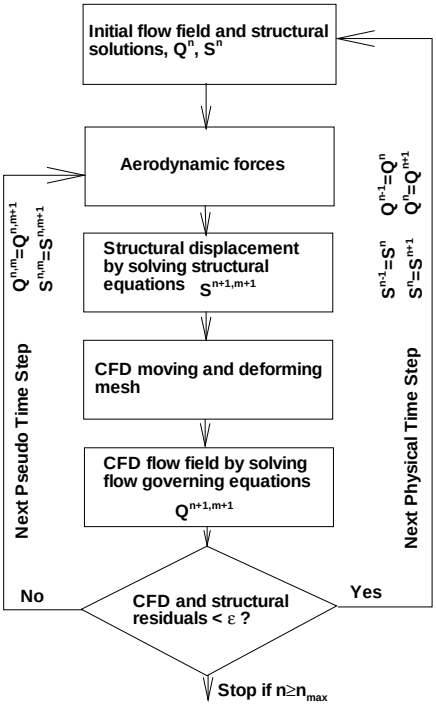

Figure 1: Fully coupled flow-structure interaction calculation procedure

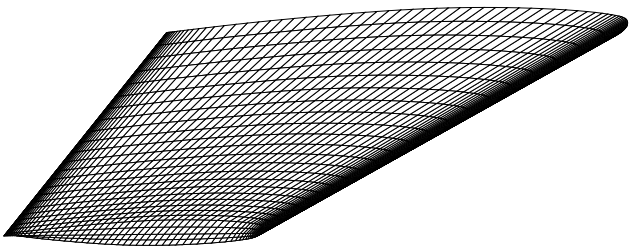

Figure 2: The mesh around the wing surface.

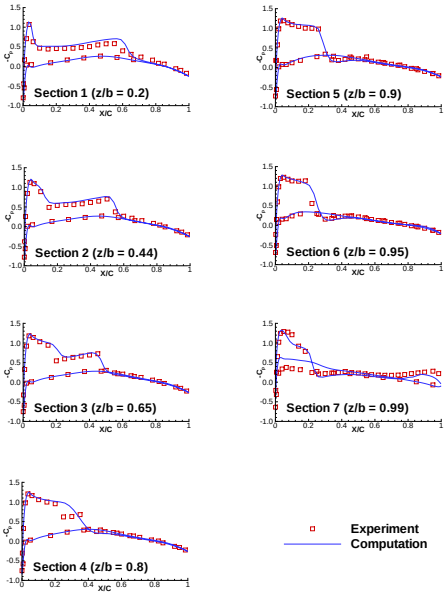

Figure 3: Pressure coefficients on the wing surface at different cross-section.

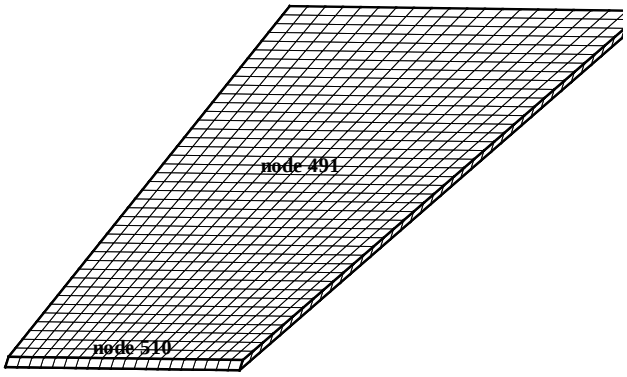

Figure 4: Plate wing geometry.

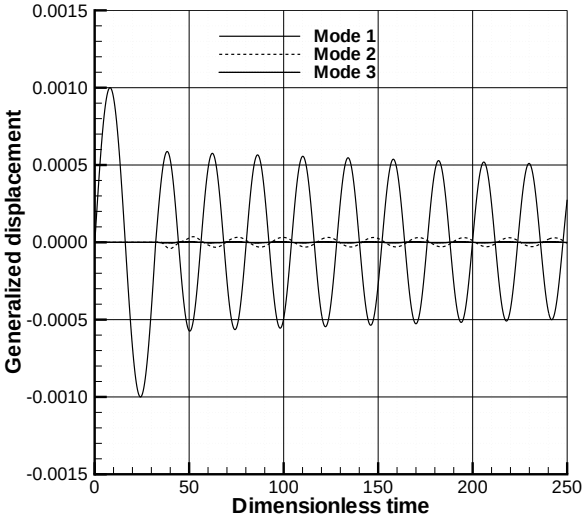

Figure 6: Time histories of the generalized displacements of first five modes for $M_\infty = 0.96$ and $V^* = 0.28$ - Damped response.

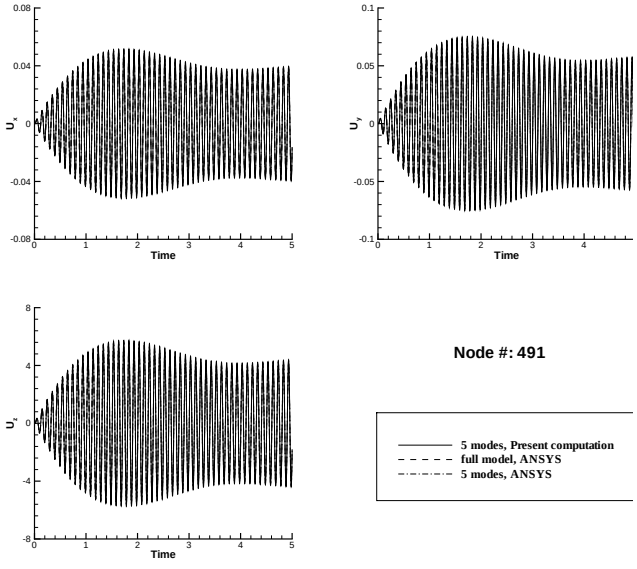

Figure 5: Histories of the dynamic responses at node point 491.

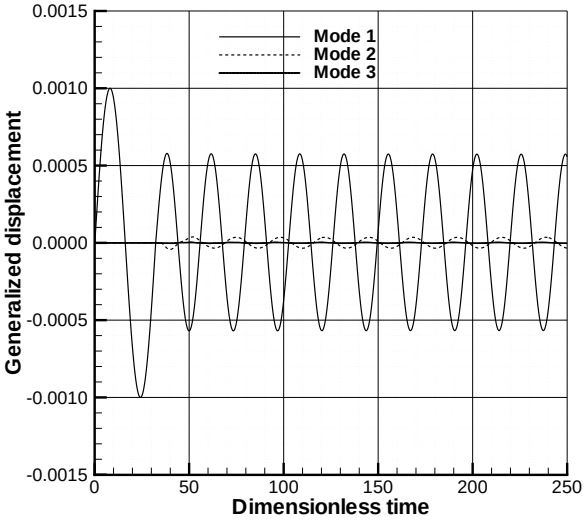

Figure 7: Time histories of the generalized displacements of first five modes for $M_\infty = 0.96$ and $V^* = 0.29$ - Neutrally stable response.

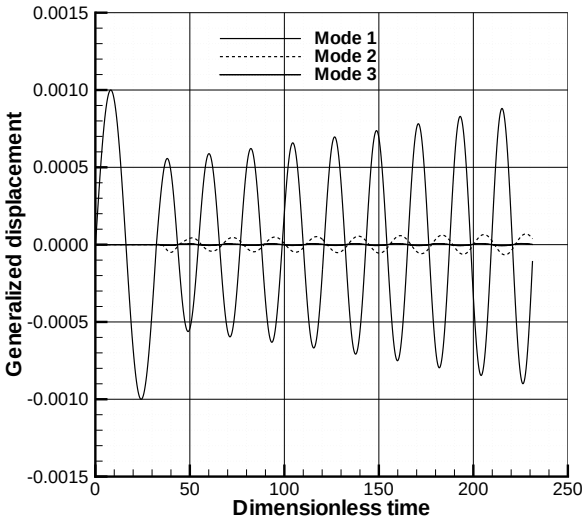

Figure 8: Time histories of the generalized displacements of first five modes for $M_\infty = 0.96$ and $V^* = 0.315$ - Diverging response.

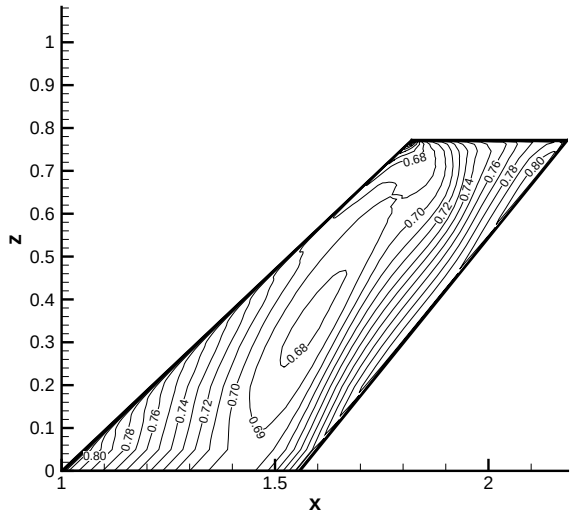

Figure 9: Pressure distribution on the wing surface when wing tip is located at uppermost position: $M_\infty = 0.96$ and $V^* = 0.29$.

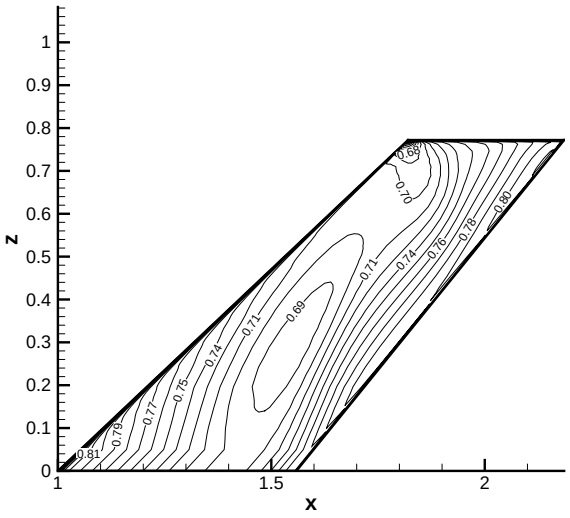

Figure 10: Pressure distribution on the wing surface when wing tip is located at neutral position: $M_\infty = 0.96$ and $V^* = 0.29$.

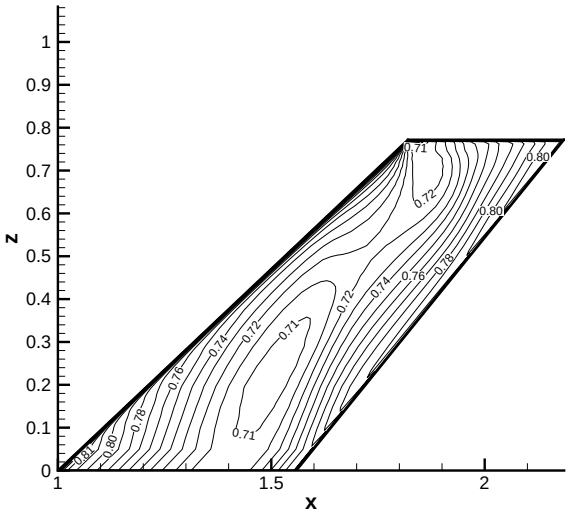

Figure 11: Pressure distribution on the wing surface when wing tip is located at lowermost position: $M_\infty = 0.96$ and $V^* = 0.29$.

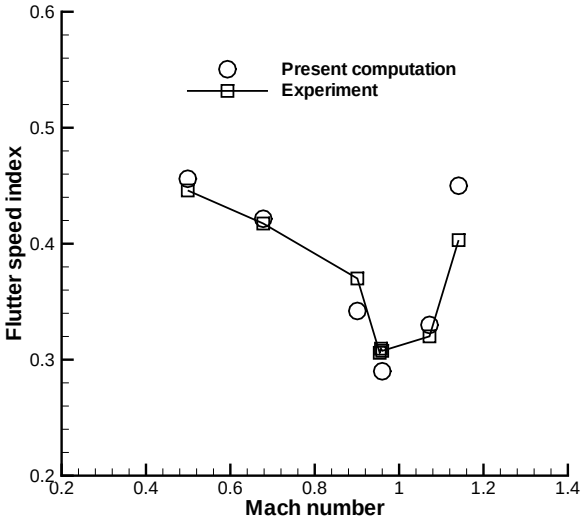

Figure 12: Comparison of computed results and experimental data for AGARD Wing 445.6.